Integrative Single-Cell Transcriptomic and Epigenomic Profiling Reveals Epigenetically Primed Gene Programs and Dynamic Switchpoints in Microglial Aging

Sean Meng[1], Emily Su[1], and Jason Buenrostro[1]

[1]Department of Stem Cell and Regenerative Biology, Harvard University, Cambridge, MA

Abstract

Aging drives progressive loss of microglial homeostatic identity and acquisition of pro-inflammatory, phagocytic phenotypes, yet the timing, chromatin basis, and regulatory drivers of this transition remain incompletely resolved. Using matched single-cell RNA-seq and bulk ATAC-seq from female C57BL/6J mouse microglia at 3, 14, and 24 months of age, we reconstruct a two-phase aging cascade: an early stress- and lipid-handling activation state followed by a late, pro-inflammatory and phagocytic conversion. Six hallmark 24-month genes (Apoe, Spp1, Ifi27l2a, Cd52, Lyz2, Cst7) show coordinated transcriptional induction and progressive chromatin opening, with ETS- and IRF-family motifs enriched at their regulatory regions, nominating PU.1, ETS1, and IRF3/8 as candidate upstream regulators. Diffusion-pseudotime reconstruction resolves a continuous aging trajectory with two sharp inflection points, homeostatic exit and aged-state commitment, each flanked by discrete switch-gene modules. This framework yields testable, gene-level hypotheses for the chromatin and transcriptional control of microglial aging and nominates specific targets for future functional perturbation.

Keywords: *microglia, aging, single-cell RNA-seq, ATAC-seq, epigenetic priming, pseudotime, neuroinflammation*

All figures referenced in the text are collected in the Figures section at the end of this article for ease of viewing at full size.

Introduction

Aging is accompanied by progressive functional and structural decline in the brain, manifesting as synaptic loss, impaired plasticity, and cognitive deficits [1]. Microglia, the resident immune cells of the central nervous system, play central roles in maintaining neural circuit integrity through synaptic pruning, debris clearance, and modulation of inflammatory signaling [2, 3]. Under homeostatic conditions, microglia express signature genes such as *P2ry12* and *Tmem119*, enabling dynamic surveillance of the parenchyma [4]. However, both rodent and human studies have revealed that aging drives mass transcriptional reorganization in microglia. Homeostatic markers fade, while interferon-stimulated genes (ISGs), MHC class I components, and pro-inflammatory cytokines become upregulated [5, 6, 7]. These molecular changes coincide with synapse engulfment, chronic neuroinflammation, and accelerated cognitive decline, implicating microglial dysregulation as a causal contributor to age-related neuropathology [8, 9].

Recent single-cell RNA-seq and ATAC-seq studies have begun to chart how microglial identity and chromatin accessibility change over the life course [10]. These studies have observed transcriptional remodeling and age-related opening of regulatory sites. Yet we still lack a detailed timeline showing when these changes occur, which transcription factors drive them, and whether discrete transition states precede terminal microglial dysfunction. Building on Li *et al.*'s publicly available, matched scRNA-seq and ATAC-seq data from female C57BL/6J mouse microglia at three, fourteen, and twenty-four months [11], we set out to answer three questions. First, what gene expression programs define the late-age, disproportionately problematic microglial states? Second, are these transcriptional changes accompanied by matching shifts in chromatin accessibility, suggesting epigenetic control? Third, can we reconstruct a continuous trajectory of microglial aging to identify molecular switchpoints that might be targeted to prevent or delay dysfunction?

To answer these questions, we implemented the following pipeline: (i) quality control and normalization of scRNA-seq data to retain high-confidence singlet microglia; (ii) identification of highly variable genes and Leiden clustering to define age-associated subpopulations; (iii) differential expression and gene-ontology analysis to characterize phase-specific transcriptional programs; (iv) differential accessibility analysis of ATAC-seq peaks to test for epigenetic priming of key genes; (v) motif enrichment to nominate candidate transcription factors driving the aged state; and (vi) diffusion-pseudotime mapping to resolve the continuous progression and uncover molecular switchpoints during aging.

Our analyses suggest a two-phase microglial aging cascade, with an early stress and lipid-handling activation followed by a late-age, pro-inflammatory, phagocytic conversion. The overlap of transcriptional shifts, accessibility gains at hallmark loci such as *Apoe*, *Spp1*, and *Ifi27l2a*, and enrichment of ETS- and IRF-family motifs together suggest epigenetic priming of the 24-month aged state. Pseudotemporal reconstruction identifies two sharp inflection points, exit from homeostasis and commitment to the aged state, each associated with candidate switch genes that may represent points for intervention. While

this framework provides mechanistic hypotheses and testable targets, functional perturbation and longitudinal *in vivo* studies will be required to establish causality and therapeutic potential.

RESULTS

To build our analyses, we utilized publicly available single-cell RNA-seq and bulk ATAC-seq datasets from 3-, 14-, and 24-month-old female mice [11].

Preprocessing

We began by imposing quality-control filters to eliminate technical artifacts and biases (Fig. 1). Barcodes were ranked by total UMI counts, and a knee inflection on the log–log curve distinguished true cells from ambient-RNA background. Symmetric thresholds on UMI counts (500–15,000) and gene counts (200–3,500) removed low-complexity or multiplet barcodes, while cells exceeding 5% mitochondrial or 50% ribosomal read fractions were excluded to avoid stressed or aberrant profiles. Scrublet further flagged high-scoring doublets for removal. A final $\log_1$ normalization yielded a homoscedastic distribution of library sizes, producing $\sim$8,000 high-confidence singlet microglia for downstream analysis.

Exploratory clustering and preliminary differential expression

To survey age-related expression changes, we identified $\sim$2,000 highly variable genes by fitting each gene's dispersion against its mean and selecting outliers (Fig. 2). Principal component analysis on these genes revealed an inflection after PC-15, so we retained PCs 1–15 for UMAP embedding. In low-dimensional space, microglia from distinct ages separate clearly. Leiden clustering at resolution 1.2 partitions cells into 18 discrete subpopulations (Fig. 2). Stacked-bar analysis showed notable shifts in cluster abundance: Cluster 0 diminishes from $\sim$40% at 3 mo to $<$10% at 24 mo, whereas Cluster 4 expands from $\sim$5% to $\sim$30% over the same interval. Pairwise differential expression (Wilcoxon rank-sum, FDR < 0.05, $|\log_2 \mathrm{FC}| > 1$) revealed a biphasic aging program: an early phase (3$\rightarrow$14 mo) marked by induction of stress and antimicrobial effectors (e.g., *S100a8*, *Ngp*, *Camp*) alongside repression of homeostatic and antigen-presentation genes (*P2ry12*, *H2-Aa*), followed by a late phase (14$\rightarrow$24 mo) in which homeostatic transcripts decrease further and phagocytic/lipid regulators (*Ltc4s*, *Fcgr3*) increase, with the full progression of homeostatic loss and inflammatory/phagocytic gain summarized across all three pairwise comparisons (Fig. 3).

Deep dive into the 24-month microglial signature

Recognizing that the aged microglial phenotype is both clinically relevant and well documented, we first characterized its molecular hallmarks (Fig. 4). Six top differentially expressed genes, *Apoe* (dysregulated lipid transport), *Spp1* (extracellular-matrix engagement), *Ifi27l2a* (chronic interferon response), *Cd52* (ectopic immunomodulation), *Lyz2* (lysosomal activation), and *Cst7* (protease inhibition), were overlaid onto UMAP, and single-cell expression distributions were quantified across ages. Each marker localizes to a discrete late-age subcluster and exhibits a significant shift in median expression (Kruskal–Wallis $p < 10^{-10}$). A complementary Gene Ontology enrichment of all 24-month upregulated genes spotlighted an interferon/cytokine axis ("response to IFN-α/γ," "innate immune response"; Fig. 5), but did not independently capture the lipid- and lysosomal-handling programs identified by our targeted marker analysis.

Epigenetic priming of aged-state genes

To test whether these transcriptional shifts are under epigenetic control, we incorporated matched bulk ATAC-seq profiles (Fig. 6). Numerous signature loci show progressive chromatin opening with age, with *Ifi27l2a* peak signal more than doubling between 14 and 24 months. This alignment between chromatin accessibility and mRNA induction indicates that key aged-state genes are likely epigenetically primed ahead of their full transcriptional activation.

Motif analysis identifies candidate upstream regulators

To nominate transcription factors that may orchestrate this chromatin remodeling, we attempted HOMER motif enrichment on $\pm$2 kb regions around 24-month ATAC-seq peaks (hypergeometric test, Benjamini–Hochberg correction; Fig. 7; see Methods for technical obstacles encountered and the workaround used). ETS-family motifs, including PU.1 (Spi1), ETS1, ELF3/5, EHF, and ERG, were highly prevalent, alongside IRF3/8 and CTCF. Although inherently correlative, these findings generate hypotheses for future perturbation (e.g., CRISPRi, CUT&RUN) to test whether these factors drive late-age microglial programs.

Pseudotemporal deconvolution reveals novel state "switchpoints"

While the 24-month phenotype reiterates known aging hallmarks, we were more interested in resolving when and how microglia transition earlier in the aging process, particularly the exit from a homeostatic state into an activated state and, eventually, into an aged/dysfunctional state. We therefore inferred a diffusion-pseudotime (DPT) trajectory from PCs 1–15 (Fig. 8a), treating pseudotime as a continuous proxy for cell-state progression. Binning pseudotime into 20 equal intervals and plotting the fraction of cells from each chronological age per bin exposed two sharply demarcated inflection points: bins 4$\rightarrow$5 and 13$\rightarrow$14, corresponding to the homeostatic-to-activated and activated-to-aged transitions, respectively (Fig. 8b,c,e).

Grouping canonical markers into functional modules, we uncovered a tightly coordinated cascade of state changes along pseudotime. Homeostatic genes collapse sharply between bins four and five just as disease-associated microglia (DAM) and activated-response microglia (ARM) signatures emerge,

while cytokine, interferon, lipid-handling, and phagocytic programs rise in concert, peaking near bins thirteen and fourteen (Fig. 8f). This inverse choreography suggests interdependent transitions rather than independent shifts and motivated a search for discrete genetic switchpoints. We defined four switch-gene modules at the homeostatic-to-activated and activated-to-aged boundaries: an early "turn-on" module of lectins and lipid enzymes (*Lgals1*, *Pla2g7*), an early "turn-off" module of homeostatic receptors (*Vcam1*), a late "turn-on" module of oxidative and phagocytic effectors (*P2ry12*, *Cybb*), and a late "turn-off" module of metabolic regulators (*Slc7a11*) (Fig. 9b). Although broad ontology terms proved uninformative for these gene sets, the precise pseudotemporal alignment of these genes highlights them as prime candidates for functional follow-up. Finally, UMAP spatial overlays showed diffuse expression beyond predicted niches, suggesting that state transitions likely require the concerted action of multiple regulators rather than a simple on/off switch (Fig. 10).

DISCUSSION

In this study, we leveraged published single-cell RNA-seq and bulk ATAC-seq data from female mice at 3, 14, and 24 months of age to build a portrait of microglial aging. Our analyses suggest that microglia traverse two distinct transcriptional phases. In the first phase, cells abandon their homeostatic surveillance program and adopt an intermediate activated phenotype. In the second phase, they fully commit to a pro-inflammatory, phagocytic state marked by dysregulated lipid handling and chronic interferon signaling. We identified gene modules whose expression turns on or off at pseudotime inflection points and uncovered motif enrichments pointing to ETS- and IRF-family transcription factors as possible regulators of the latter, aged transition.

These findings provide a structured hypothesis framework, but they remain provisional. Our conclusions rest entirely on correlative analysis of existing datasets and may be influenced by technical artifacts, batch effects, or unmeasured variables in the original experiments. We cannot yet claim that any individual transcription factor or switch gene is required or sufficient to drive microglial state transitions *in vivo*. Definitive validation will require targeted perturbations, such as CRISPRi or inducible knockouts of candidate transcription factors and switch genes. Likewise, CUT&RUN or ChIP-seq experiments will be needed to confirm binding of PU.1, ETS1, IRF3, and other candidate factors at predicted regulatory elements in microglia across ages.

To strengthen the epigenetic dimension of our model, single-cell ATAC-seq profiling of microglia from young, mid-age, and old mice would enable direct linkage of chromatin accessibility changes to individual cells and clusters. Integration of single-cell multiome (combined RNA and ATAC) data would further reveal how transcriptional and epigenetic states coevolve, improving the resolution of the switchpoints inferred here by pseudotime. Functional assays will also be essential for connecting state transitions to microglial behavior: *ex vivo* phagocytosis assays, lipid-uptake measurements, and cytokine-release profiling could quantify the functional impact of switch-gene perturbation, while longitudinal two-photon imaging of microglial process dynamics would directly assess whether candidate interventions preserve surveillance behavior and prevent age-associated synaptic loss.

Looking forward, sex differences represent a critical but unaddressed variable. Existing literature suggests that male microglia may bypass the intermediate activation stage entirely, progressing directly from a youthful to an aged state. Comparative analysis of male and female microglial single-cell transcriptomes, together with circulating sex hormone measurements, could clarify how estrogen, progesterone, and testosterone modulate the timing and trajectory of these state transitions.

We also lack clarity on the upstream triggers of microglial reprogramming. Emerging evidence implicates age-associated loss of heterochromatin and derepression of repetitive elements, leading to cytosolic accumulation of double-stranded RNA and activation of the RIG-I/MAVS pathway, which could in turn drive interferon secretion and microglial overactivation. This hypothesis could be tested by measuring expression of sensors such as *Mavs* and *Ifih1*, together with endogenous retroelement transcripts, in single-cell data, and through *in vitro* experiments in which cultured microglia are treated with synthetic dsRNA or subjected to genetic manipulation of heterochromatin regulators (for example, overexpression of HP1α) to test whether limiting dsRNA accumulation attenuates the aged transcriptional program.

Taken together, our analysis offers a hypothesis-driven roadmap for future work. By combining targeted perturbation of candidate regulators, single-cell multiomic profiling, sex-comparative studies, and functional assays of microglial behavior, we can move from descriptive correlations toward mechanistic understanding and, ultimately, toward strategies for maintaining microglial homeostasis and mitigating neuroinflammation in aging.

METHODS

Data sources

We reanalyzed publicly available datasets from female C57BL/6J mice at 3, 14, and 24 months of age. Single-cell RNA-seq data (GEO: GSE208346) comprised six 10x Genomics libraries (two biological replicates per age). Matched bulk ATAC-seq narrowPeak and bigWig files were obtained from the same study. All code was executed in Python 3.9, using Scanpy v1.9.1 for transcriptomic workflows, Scrublet v0.2.3 for doublet detection, pyBigWig v0.3.18 for ATAC-seq quantification, and HOMER v4.11 for motif analysis.

Single-cell RNA-seq preprocessing

Raw UMI counts were loaded into an AnnData object. Per-cell QC metrics, total UMIs, genes detected, mitochondrial fraction (genes prefixed "MT-"), and ribosomal fraction (genes matching `^RPS|^RPL`), were computed. Scrublet assigned doublet scores assuming a 5% expected doublet rate. We retained

cells meeting all of the following: 1,000 $\leq$ UMIs $\leq$ 15,000; 500 $\leq$ genes detected $\leq$ 3,500; mitochondrial reads $<$ 10%; ribosomal reads $<$ 10%; doublet score $<$ 0.20. Filtered counts were normalized to 10,000 counts per cell and $\log_1$-transformed; raw counts were stored in `.raw` for downstream differential expression.

Feature selection, dimensionality reduction, and clustering

We identified $\sim$2,000 highly variable genes by fitting normalized dispersion against mean expression and selecting outliers above the trend. Data were scaled to unit variance (clipped at ± 10) prior to PCA; we retained the first 15 PCs, selected by an elbow in the variance-ratio plot. A k-nearest-neighbors graph ($k = 15$) on these PCs underlay Leiden clustering at resolution 0.6 for initial partitioning. UMAP embeddings were computed with default Scanpy parameters. To focus on peripheral blood ("PB") microglia samples, we subset those cells and reclustered at resolution 1.2.

Differential expression and enrichment

Pairwise differential expression between ages, and between pseudotime bins, used Scanpy's Wilcoxon rank-sum test (`tl.rank_genes_groups`) with Benjamini–Hochberg correction (FDR < 0.05) and $|\log_2 \mathrm{FC}| > 1$. Volcano and dot plots highlighted key markers. For Gene Ontology enrichment of 24-month upregulated genes, we submitted the differentially expressed gene list to Enrichr via `gseapy`, testing against the GO Biological Process library and ranking terms by $-\log_{10}$(adjusted p-value).

Bulk ATAC-seq analysis

We developed and tested a complete Python pipeline to requantify chromatin accessibility over a custom consensus peak set. Six narrowPeak files (two replicates per age) were concatenated, sorted by chromosome and start coordinate, and merged into a non-redundant peak set. Using pyBigWig, each bigWig file was queried to sum per-base coverage over every consensus peak, producing a $6 \times N$ matrix of raw counts. Counts were normalized to counts per million (CPM), $\log_1$-transformed, and passed to DESeq2 via `rpy2` to identify age-dependent differential accessibility (FDR < 0.05, $|\log_2 \mathrm{FC}| > 1$). Motif enrichment and differential-accessibility results reported in the main text for genes induced at 24 months (Figs. 6–7) reflect the previously published ATAC-seq analysis of this dataset (Supplementary Data 6 of Li *et al.* [11]), used here as a validated reference in place of the custom pipeline described above.

REFERENCES

[1] Morrison, J. H. & Baxter, M. G. The ageing cortical synapse: hallmarks and implications for cognitive decline. *Nat. Rev. Neurosci.* **13**, 240–250 (2012).

[2] Salter, M. W. & Stevens, B. Microglia emerge as central players in brain disease. *Nat. Med.* **23**, 1018–1027 (2017).

[3] Nimmerjahn, A., Kirchhoff, F. & Helmchen, F. Resting microglial cells are highly dynamic surveillants of brain parenchyma *in vivo*. *Science* **308**, 1314–1318 (2005).

[4] Butovsky, O. *et al.* Identification of a unique TGF-β–dependent molecular and functional signature in microglia. *Nat. Neurosci.* **17**, 131–143 (2014).

[5] Galatro, T. F. *et al.* Transcriptomic analysis of purified human cortical microglia reveals age-associated changes. *Nat. Neurosci.* **20**, 1162–1171 (2017).

[6] Holtman, I. R. *et al.* Induction of a common microglia gene expression signature by aging and neurodegenerative conditions: a co-expression meta-analysis. *Acta Neuropathol. Commun.* **3**, 31 (2015).

[7] Corces, M. R. *et al.* Lineage-specific and single-cell chromatin accessibility charts human hematopoiesis and leukemia evolution. *Nat. Genet.* **51**, 1208–1219 (2019).

[8] Streit, W. J., Xue, Q. S. & Bechmann, I. Dystrophic microglia in late-onset Alzheimer's disease. *Glia* **62**, 1630–1639 (2014).

[9] Raj, D. *et al.* Increased white matter inflammation in aging- and Alzheimer's disease brain drives differential Aβ plaque clearance and impacts the immune response. *Acta Neuropathol.* **134**, 662–681 (2017).

[10] Hammond, T. R. *et al.* Single-cell RNA sequencing of microglia throughout the mouse lifespan and in the injured brain reveals complex cell-state changes. *Immunity* **50**, 253–271.e6 (2019).

[11] Li, X. *et al.* Transcriptional and epigenetic decoding of the microglial aging process. *Nat. Aging* **3**, 1288–1311 (2023).

FIGURES

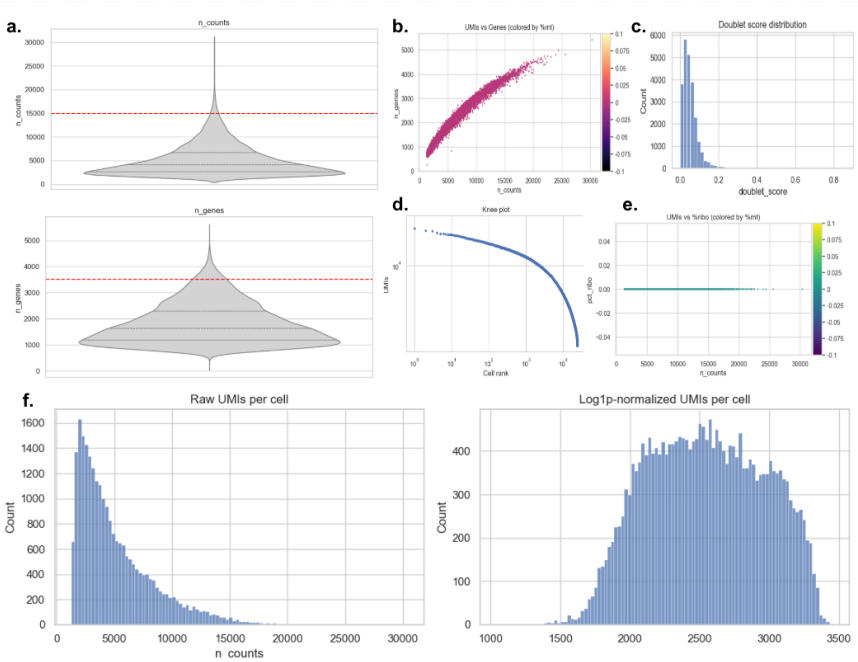

Figure 1: Quality control and normalization of microglial single-cell RNA-seq. (a) Violin plots of UMI counts (1,000–15,000) and detected genes (500–3,500) with inclusion thresholds. (b) UMI vs. gene-count scatter colored by % mitochondrial reads; cells >10% mt removed. (c) Scrublet doublet-score histogram; cells ≥0.20 excluded. (d) Log–log "knee" plot of ranked UMIs defining true cells vs. ambient RNA. (e) UMI vs. % ribosomal reads scatter; cells >10% ribo discarded. (f) Raw vs. $\log_1$-normalized UMI distributions, showing removal of extremes and a homoscedastic profile for downstream analysis.

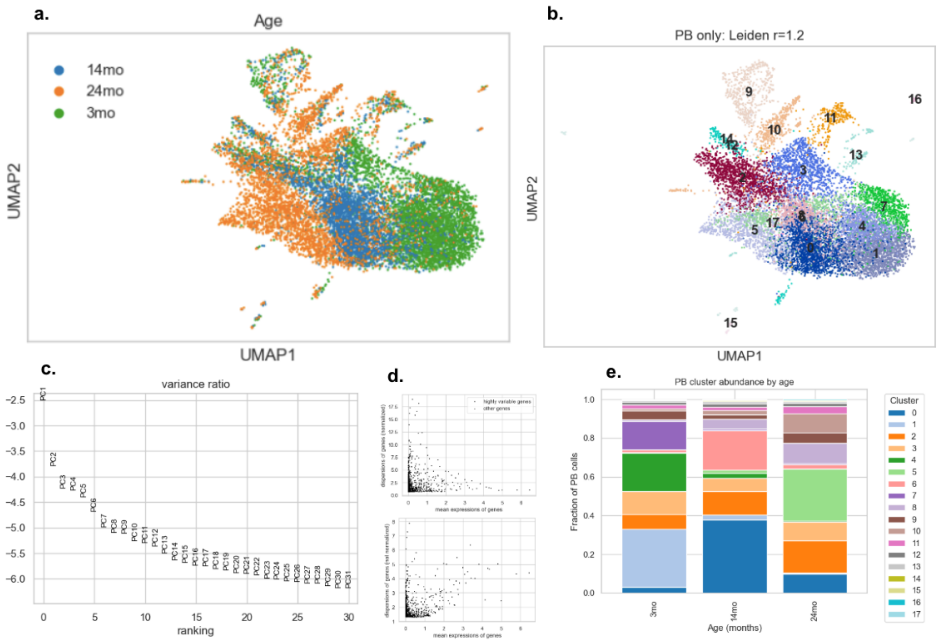

Figure 2: Dimensionality reduction and clustering of microglial single-cell transcriptomes. (a) UMAP of QC-filtered microglia colored by age (3 mo = green, 14 mo = blue, 24 mo = orange), showing clear age-dependent separation. (b) UMAP of the PB subset with Leiden clustering (resolution 1.2), defining 18 clusters (0–17). (c) Scree plot of PCA variance; PCs 1–15 (pre-elbow) were used for graph construction and UMAP. (d) Mean-dispersion plot selecting ∼2,000 highly variable genes above the threshold curve. (e) Stacked bar plots of cluster fractions at 3, 14, and 24 mo, illustrating loss of Cluster 0 and expansion of Cluster 4 with age.

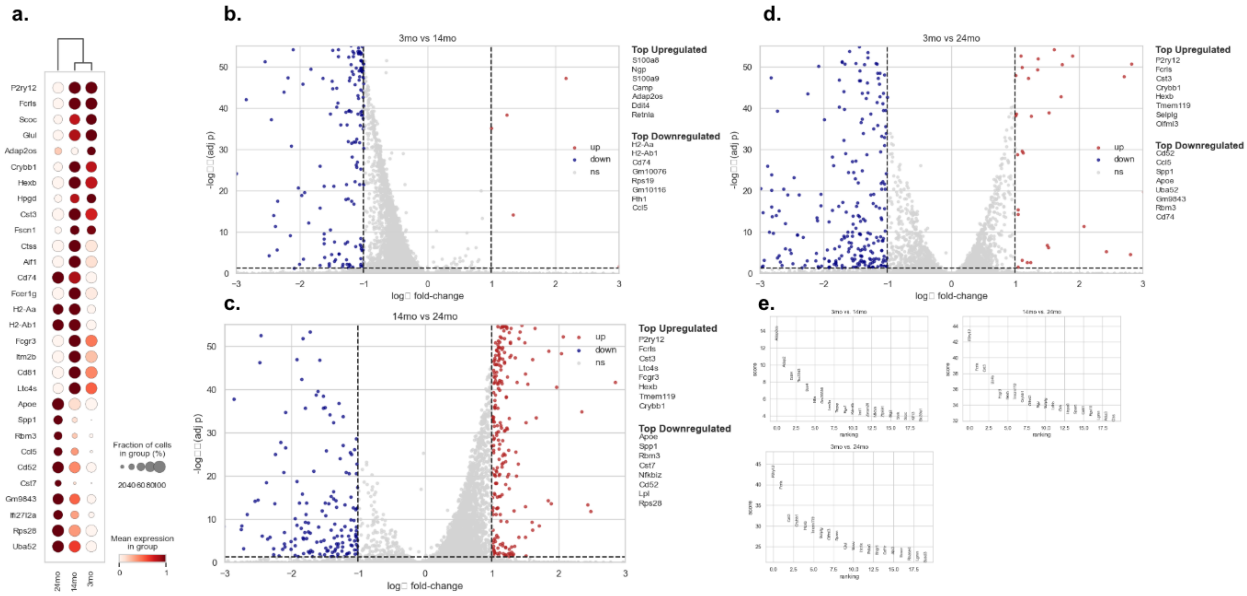

Figure 3: Stepwise loss of homeostatic signatures and gain of inflammatory/phagocytic programs during microglial aging. (a) Dot plot of homeostatic (*P2ry12*, *Fcrls*, *Tmem119*) versus activation (*Apoe*, *Spp1*, *Ctss*) markers at 3, 14, and 24 mo; dot size shows percent expressing cells and color shows the z-scored mean. (b–d) Volcano plots for 3 vs. 14 mo (b), 14 vs. 24 mo (c), and 3 vs. 24 mo (d) (Wilcoxon, FDR < 0.05, $|\log_2 \mathrm{FC}| > 1$), with key up- and down-regulated genes indicated. (e) Bar charts of the top ten most significant up- and down-regulated genes in each comparison ($-\log_{10}$ adj. p).

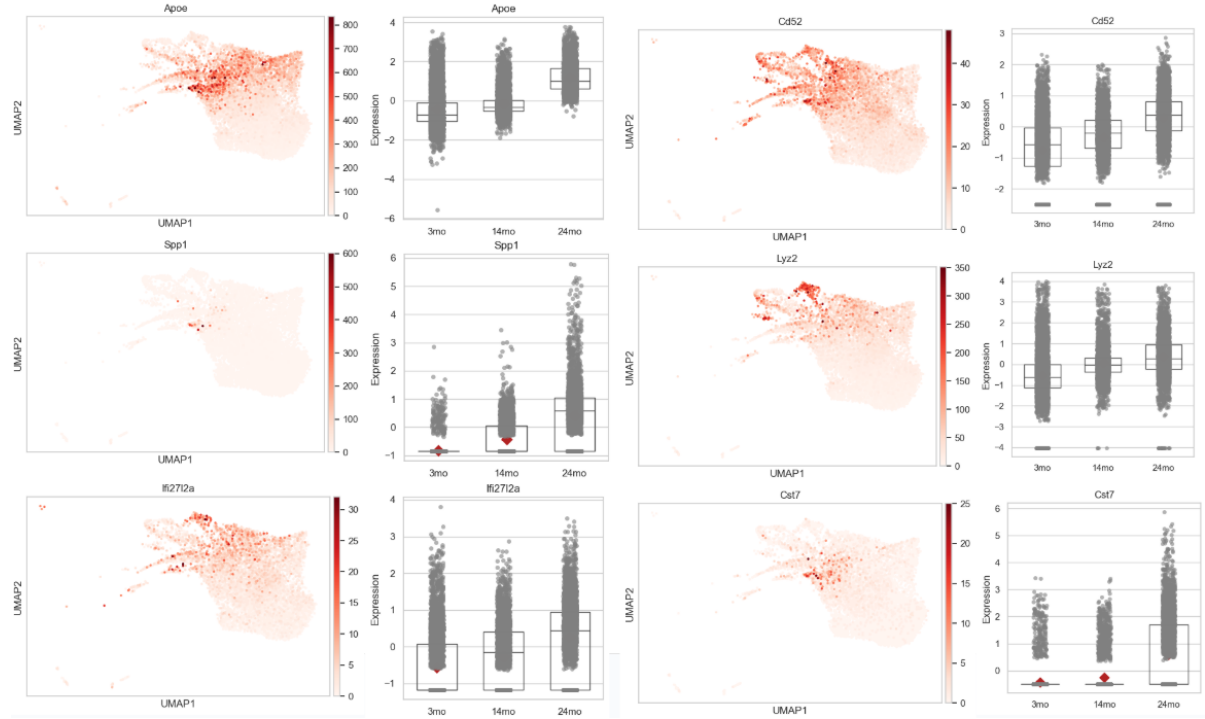

Figure 4: Single-cell expression of six hallmark 24-month microglial markers. Each row shows one of the top six genes, *Apoe*, *Spp1*, *Ifi27l2a*, *Cd52*, *Lyz2*, and *Cst7*, mapped onto the UMAP embedding as a continuous heatmap, with darker shades indicating higher $\log_1$ expression. To the right of each heatmap, jittered scatter and box plots summarize per-cell expression at 3, 14, and 24 months (boxes = median $\pm$ IQR; whiskers = 1.5$\times$IQR; points show individual cells). All six markers are largely restricted to late-age clusters and undergo highly significant induction with age (Kruskal–Wallis $p < 1 \times 10^{-10}$).

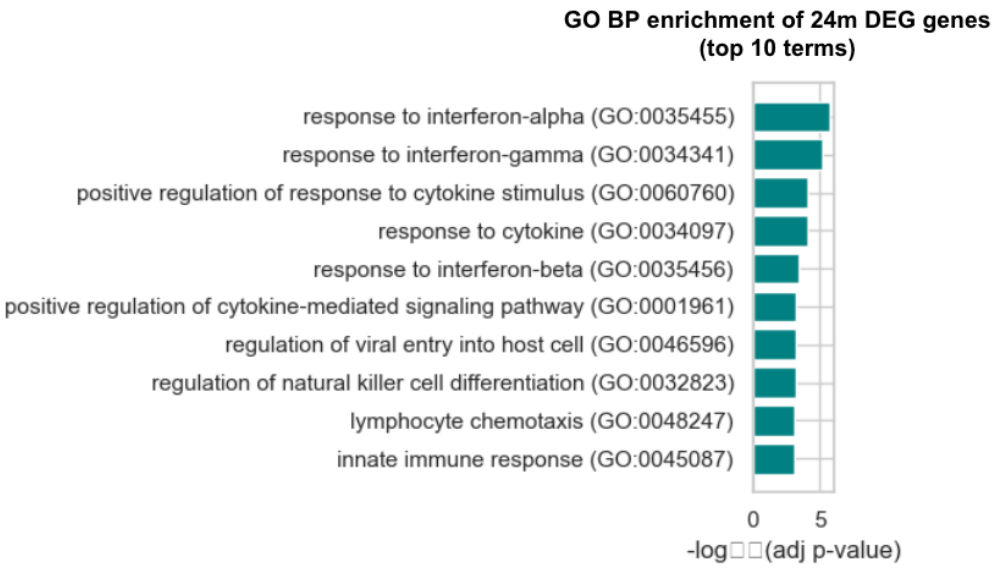

Figure 5: Gene Ontology enrichment of 24-month upregulated microglial genes reveals interferon- and cytokine-driven activation programs. Bar plot of the ten most significantly overrepresented GO Biological Process terms among genes upregulated at 24 months (FDR < 0.05, $|\log_2 \mathrm{FC}| > 1$), ranked by $-\log_{10}$(adjusted p-value). Top hits include "response to interferon-alpha," "response to interferon-gamma," "positive regulation of response to cytokine stimulus," and "innate immune response," demonstrating a shift toward sustained interferon and cytokine signaling in aged microglia.

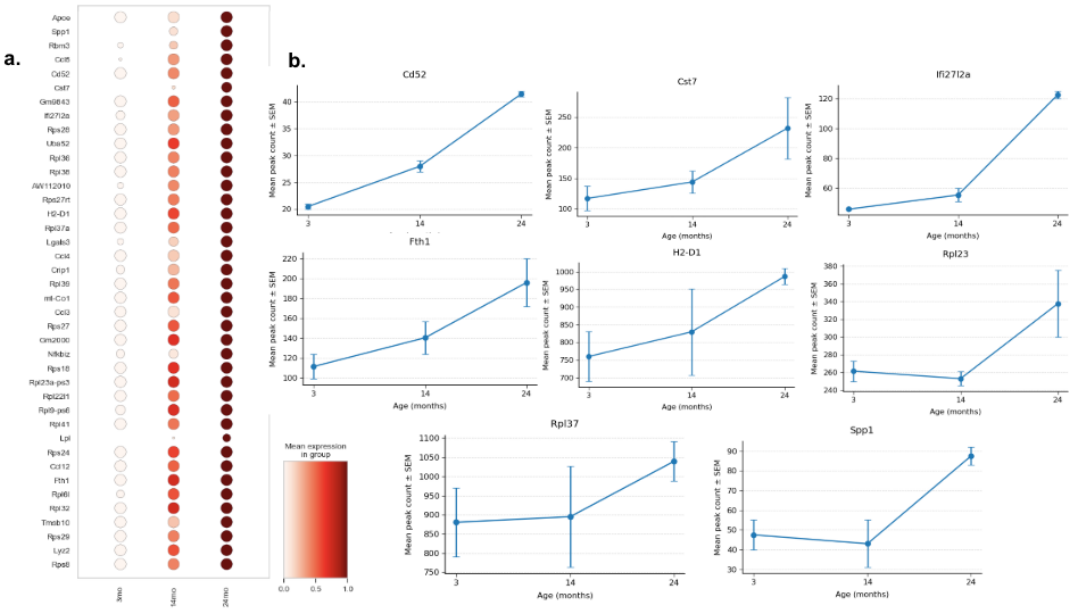

Figure 6: Expression and chromatin accessibility changes at late-age microglial genes. (a) Bubble plot of the top 50 genes upregulated at 24 mo (Wilcoxon FDR < 0.05, $|\log_2 \mathrm{FC}| > 1$), showing mean log-normalized expression (color) and fraction of cells expressing each gene (size) at 3, 14, and 24 mo. *Apoe*, *Spp1*, *Cd52*, *Cst7*, and *Ifi27l2a* are largely confined to the 24-mo state. (b) Mean $\pm$ SEM normalized ATAC-seq counts for eight representative loci (*Cd52*, *Cst7*, *Ifi27l2a*, *Fth1*, *H2-D1*, *Rpl23*, *Rpl37*, *Spp1*) at 3, 14, and 24 mo, illustrating modest mid-age increases and steep accessibility gains by late age (e.g., *Ifi27l2a* $>2\times$; *Cd52* $>50\%$).

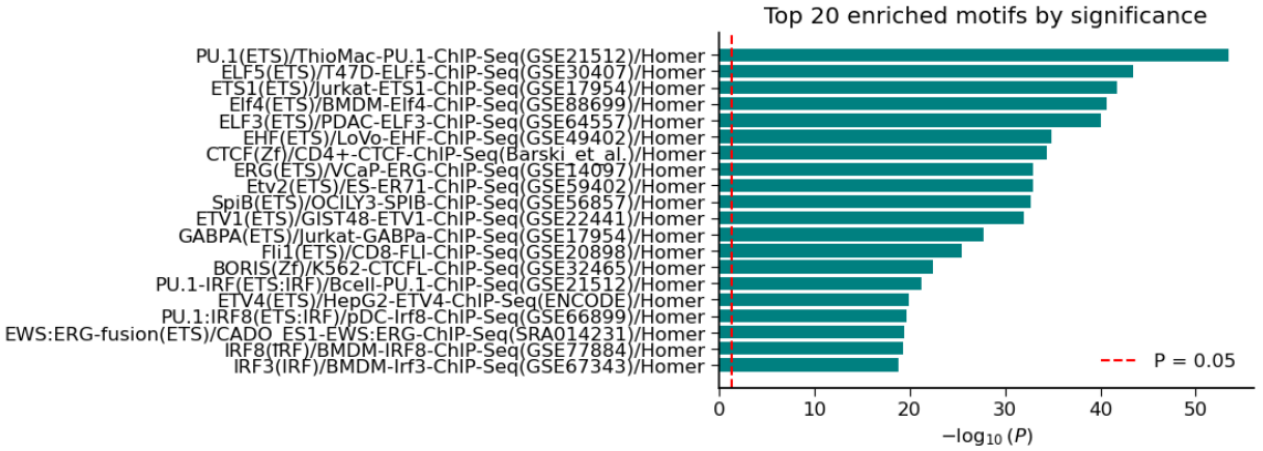

Figure 7: Enrichment of ETS- and IRF-family motifs in ATAC-seq peaks linked to 24-month upregulated genes. Motif over-representation results were taken from the published ATAC-seq analysis (Supplementary Data 6) for peaks ± 2 kb from the TSS of genes induced at 24 months (FDR < 0.05, $|\log_2 \mathrm{FC}| > 1$). Bars show the top 20 motifs ranked by $-\log_{10}(p)$. ETS-family sites, including PU.1/Spi1, ELF5, ETS1, ELF3, EHF, and ERG, are most enriched, followed by IRF3/8 and CTCF.

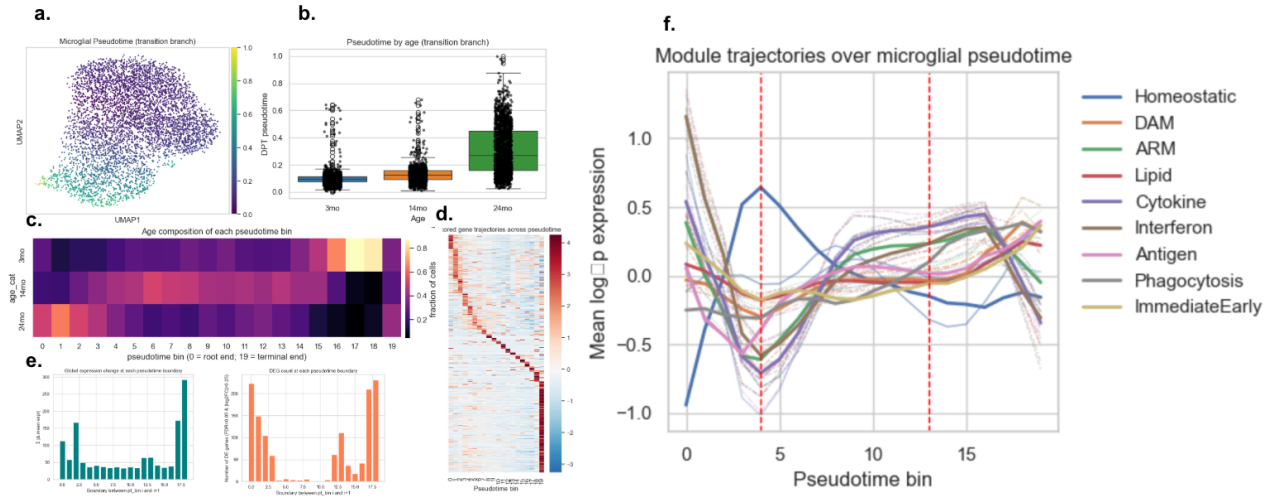

Figure 8: Pseudotime ordering defines two major transcriptional switchpoints in microglial aging. (a) UMAP colored by DPT pseudotime. (b) Pseudotime distributions by age (3, 14, 24 mo). (c) Age composition across 20 pseudotime bins. (d) Heatmap of differentially expressed genes ordered by peak pseudotime bin. (e) Boundary metrics; the sum of expression change and DEG count peak at bins 4→5 and 13→14. (f) Module trajectories: homeostatic collapse at the first switch, a transient DAM/ARM peak, and inflammatory/lipid induction at the second.

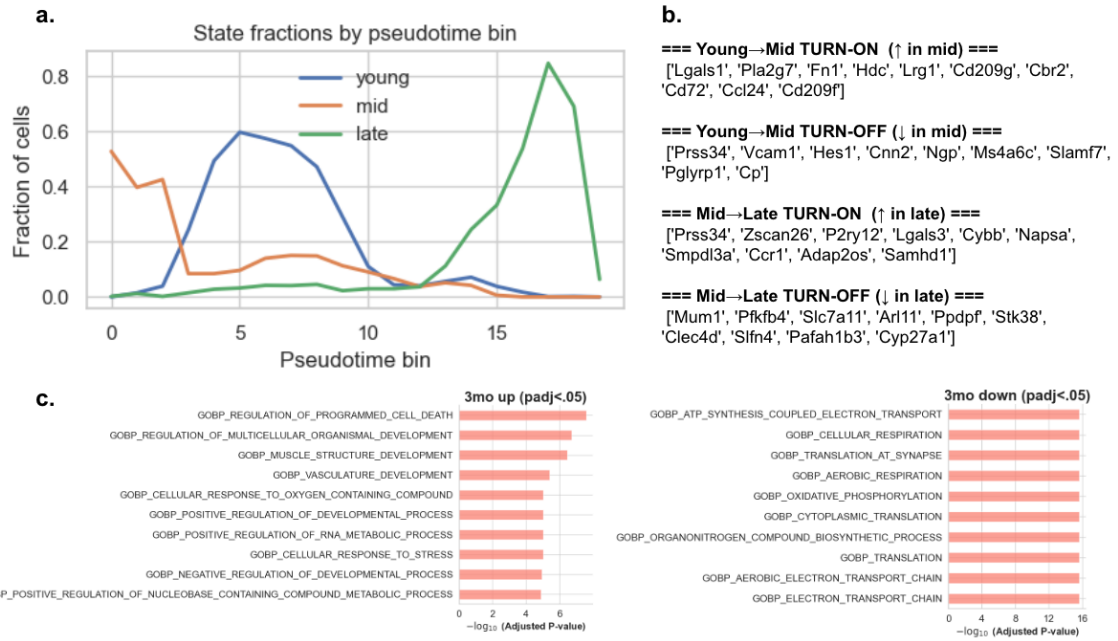

Figure 9: Molecular "switch" genes at two pseudotime transitions. (a) Line plots of age composition (3 mo = blue, 14 mo = orange, 24 mo = green) across 20 DPT bins reveal two sharp crossovers at bins 4→5 and 13→14, marking homeostatic→activated and activated→aged transitions. (b) Differential expression between bins 4 vs. 5 and 13 vs. 14 (FDR < 0.05, $|\log_2 \mathrm{FC}| > 1$) defines four gene modules: young→mid turn-on (e.g., *Lgals1*, *Pla2g7*), young→mid turn-off (e.g., *Prss34*, *Vcam1*), mid→late turn-on (e.g., *P2ry12*, *Cybb*), and mid→late turn-off (e.g., *Slc7a11*, *Mum1*). (c) GO-BP overrepresentation for the two turn-on sets yields only broad terms (e.g., programmed cell death, oxidative phosphorylation), underscoring that these switch-gene lists provide the most precise hypotheses for follow-up.

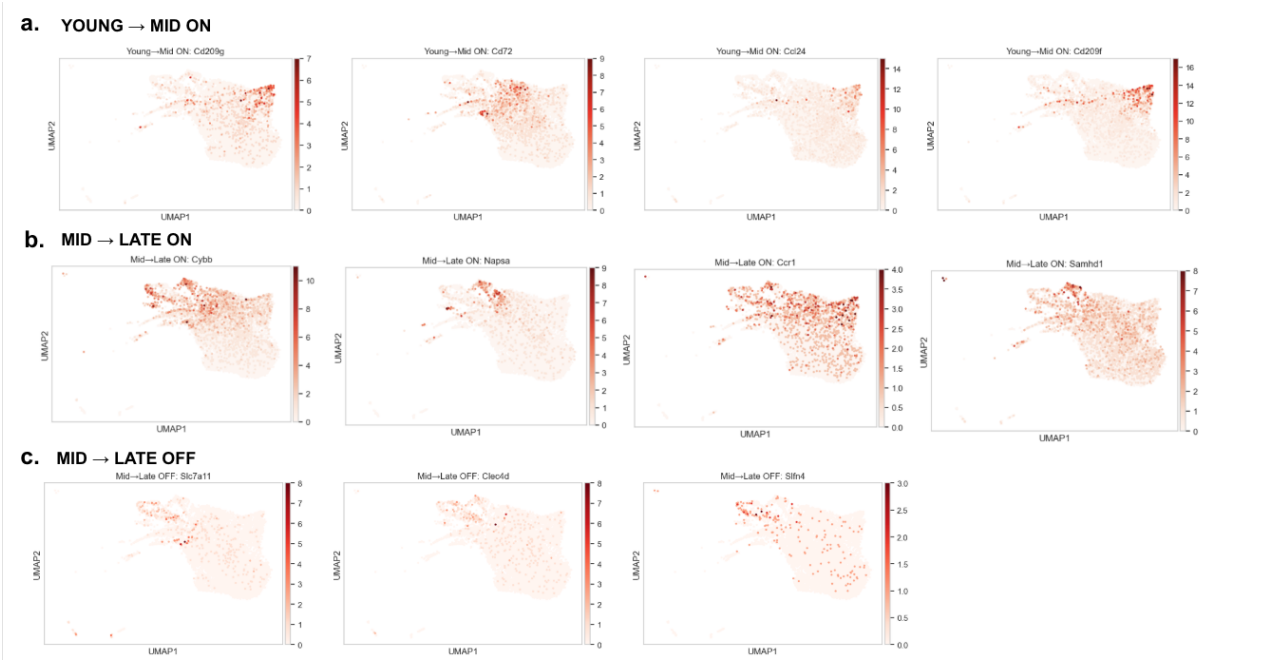

Figure 10: Spatial UMAP overlays of pseudotime "switch" genes reveal graded expression patterns. (a) Young→mid turn-on genes (*Cd209g*, *Cd72*, *Ccl24*, *Cd209f*) are enriched in mid-trajectory clusters but remain detectable elsewhere. (b) Mid→late turn-on genes (*Cybb*, *Napsa*, *Ccr1*, *Samhd1*) peak in the terminal aged cluster yet show background levels upstream. (c) Mid→late turn-off genes (*Slc7a11*, *Clec4d*, *Slfn4*) decline progressively rather than abruptly toward the end of the trajectory.